ADVANCED MATERIALS
www.advmat.de

A Wearable Microneedle-Based Extended Gate Transistor for Real-Time Detection of Sodium in Interstitial Fluids

Youbin Zheng, Rawan Omar, Rongjun Zhang, Ning Tang, Muhammad Khatib, Qi Xu, Yana Milyutin, Walaa Saliba, Yoav Y. Broza, Weiwei Wu, Miaomiao Yuan, and Hossam Haick**

Sodium is a prominent prognostic biomarker for assessing health status, such as dysnatremia. As of now, detection and monitoring of sodium levels in the human body is carried out by means of laborious and bulky laboratory equipmentand/or by offline analysis of various body fluids. Herein, an innovative stretchable, skin-conformal and fast-response microneedle extended-gate FET biosensor is reported for real-time detection of sodium in interstitial fluids for minimally invasive health monitoring along with high sensitivity, low limit of detection, excellent biocompatibility, and on-body mechanical stability. The integration of the reported device with a wireless-data transmitter and the Internet-of-Things cloud for real-time monitoring and long-term analysis is reported and discussed. This platform would eventually help bringing unlimited possibilities for effecient medical care and accurate clinical decision-making.

Y. Zheng, R. Omar, N. Tang, M. Khatib, Y. Milyutin, W. Saliba, Y. Y. Broza, H. Haick
Department of Chemical Engineering and Russell Berrie Nanotechnology Institute
Technion-Israel Institute of Technology
Haifa 3200003, Israel
E-mail: hhossam@technion.ac.il

R. Zhang, M. Yuan
The Eighth Affiliated Hospital
Sun Yat-sen University
Shenzhen 518033, P. R. China
E-mail: yuanmm3@mail.stsu.edu.cn

R. Zhang
Institute of Molecular Medicine (IMM)
Renji Hospital
Shanghai Jiao Tong University School of Medicine
Shanghai 200240, P. R. China

Q. Xu
Institute of Nanoscience and Nanotechnology
School of Materials and Energy
Lanzhou University
Lanzhou 730000, P. R. China

W. Wu, H. Haick
School of Advanced Materials and Nanotechnology
Interdisciplinary Research Center of Smart Sensors
Xidian University
Xi'an 710126, P. R. China

The ORCID identification number(s) for the author(s) of this article can be found under https://doi.org/10.1002/adma.202108607.

DOI: 10.1002/adma.202108607

1. Introduction

Sodium is a prominent prognostic biomarker for assessing health status. An imbalance in sodium concentration, termed dysnatremia, includes hyponatremia (bellow 135 mmol L^{-1})[1] and hypernatremia (more than 145 mmol L^{-1})[2,3] and is considered one of the most prominent predictors for mortality and morbidity in hospitalized patients and patients in intensive care units (ICUs).[4–6] One-third of elderly patients admitted to the emergency room and one-third of critically ill patients admitted to ICU suffer from dysnatremia.[7] It has been proved that dysnatremia could work as a major prognostic factor in patients with heart failure,[8–11] Coronavirus (COVID-19),[12–14] and chronic kidney disease,[15,16] impacting both short- and long-term outcomes.[17] Therefore, it is crucial to assess the patient's health by regularly measuring the sodium levels.

As of now, sodium analysis from body fluids relies on collecting samples followed by offline analysis, which is laborious and involves bulky laboratory equipment. Therefore, these systems do not allow continuous measurements of fluid composition, putting serious restrictions, especially in the emergency room and ICU where patients are very sick and even unconscious. On the other hand, the current clinical method to measure sodium levels is by electrolyte panel blood test, which is not only painful, but also time-consuming to perform. More importantly, this method requires specialists and does not provide continuous measurements. Other commercial devices found in the market include two main platforms. The first is based on ion selective electrodes (e.g., HORIBA Laqua Twin Salt meter, Hach Intellical probe). These devices can offer portable sodium testing with high accuracy and fast response. However, they require time-consuming and complicated sample preprocessing phase for extraction of body fluid (e.g., sweat, blood, and interstitial fluids [ISF]), thus inhibiting the possibility of online monitoring. The second group includes flame photometer. Although highly accurate, this instrument is expensive and not portable, requires expert personnel to operate, and is used for offline measurements only.

Wearable devices based on sweat or ISF biosensing[18–20] have considerable advantage in monitoring (e.g., through perspiration) multi-physiological indexes and biomarkers[21,22] (e.g.,

minerals, trace elements, lactic acid, urea, and volatile organic compounds). Compared to blood, ISF should be easier, painless, and give safer online and in situ biomarker analysis for long-term monitoring.[23] Furthermore, it eliminates the need for extraction methods or dealing with blood clots. Compared to sweat, especially for ill or elderly patients, ISF could provide biomarker analysis without the need for excessive sweating exercises or being affected by confounding factors linked with the sweat conditions, such as poor sweat rates, sample evaporation, sample freshness, and/or contamination from the skin.[24,25] One of the highly effective approaches to measure sodium levels without pain inside the ISF is the use of microneedles (MNs).[26–29] Nevertheless, most common MNs are typically constrained to rigid structures, challenging their use in stretchable or flexible devices. Indeed, the design and development of flexible MN devices has been challenged by low mechanical stability and breakability upon attachment to skin, making them unsuitable for long-term monitoring or for real-life clinical applications.[30–32] Taking advantages of field-effect transistor (FET), extended gate (EG) FET-based biosensors can achieve fast response, low-cost scalability, high stability, durability, and longer-lasting use. [33,34]

Here, we report a novel stretchable, stable, biocompatible, and minimally invasive biosensor design for continuous and real-time detection of sodium for health monitoring. The device relies on a new architecture of FETs whose sensing part and reference electrode rely on extended gate (EG) made of MNs that penetrate the skin to reach the ISF or measuring the sodium therein. The electrical response of the reported sensors over sodium concentration, repeatability and selectivity were conducted to characterize their performance. The mechanical stability of the platform was also evaluated by on-body experiments and the response recorded over MNs inserting and peeling-off cycles. In vitro and in vivo biocompatibility experiments of the MNs were validated to prove their function in transnational clinical and on-body applications. Finally, the MN-EGFET platform were integrated with wireless data transmission including Internet-of-Things (IoT) cloud, and clinical real-time measurements were recorded in comparison to a commercial reference device.

2. Results

2.1. Concept, Device Architecture, and Fabrication of the MN-EGFET

For real-time and continuous measurement of sodium concentration, MN-EGFET was designed and fabricated (**Figure 1**a and Figure S1, Supporting Information). The MN-EGFET is comprised of two main parts: a replaceable MNs sensing part and a reusable FET transducer (Figure 1b). Figure 1c shows the stretchable sensing MNs, which combines the rigid MNs' EG, reference electrode (RE) and silver nanowires (AgNWs) electrodes. Solid polystyrene (PS) MNs were fabricated by poly(dimethylsiloxane) (PDMS) molds. A thin layer of titanium

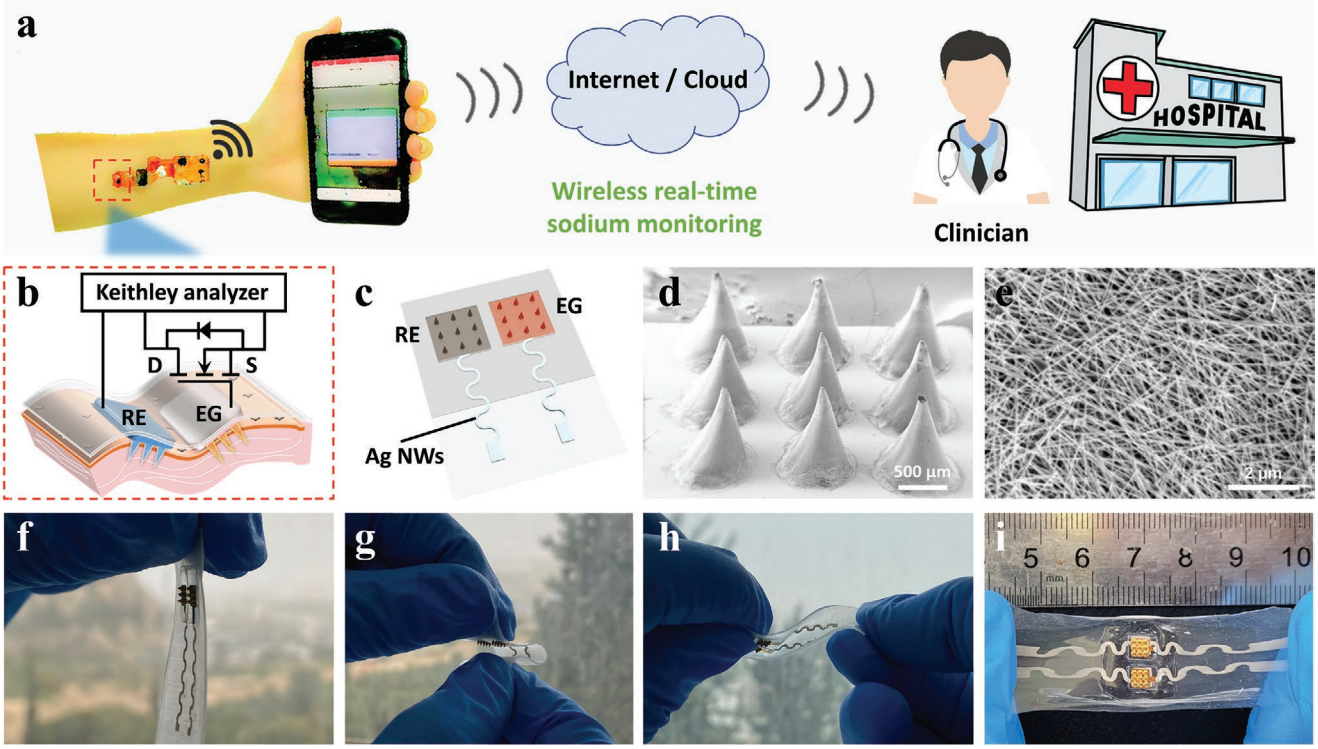

Figure 1. Design and fabrication of the MN-EGFET biosensing platform. a) Concept of real-time wireless monitoring of sodium levels using smartphone integrated with IoT technologies. b) Schematic of the MN-EGFET platform and the measurement system. c) Illustration of the stretchable extended gate MNs and reference MNs. d) SEM image of the fabricated MNs. e) SEM image of sprayed AgNWs electrodes. f–h) Photos of stretchable MN-loaded patch showing good flexibility with bending and twisting. i) Stretching of the rigid MN-loaded thickness-gradient SIS film.

(Ti) (10 nm) was then deposited as an adhesion layer before gold (Au) was deposited onto the PS microneedle substrate. Ag was deposited on one of the other MN electrodes to be used as a reference electrode (Figure S1a, Supporting Information). Each MN is conical with a 10 µm radius of curvature at the tip, ≈750 µm in diameter at the base, and ≈1000 µm in height (Figure 1d and Figure S2, Supporting Information). For different analyte detection, the EG can be modified with different biorecognition elements, including ion-selective membrane (ISM), enzyme and antibody. For demonstrating the MN-EGFET's design concept , sodium-selective membrane was chosen to detect sodium (Na^+) analyte. In this design, the MNs enable accessibility to the ISF's sodium and controllability of the FET's mode of operation in real-time, without the need for extraction methods or any excessive activities. Subsequently, the concentration input is transduced to an electric signal by the FET. The output can be directly transferred to doctors and clinics via smartphone/computer integrated with IoT technologies (Figure 1a).

To fabricate the stretchable MN-EG, AgNWs were spray-coated and transferred onto styrene-*block*-isoprene-*block* styrene (SIS) soft stretchable substance using a mask forming stretchable electrodes (Figure S1b, Supporting Information). Due to their network structure (Figure 1e) and high conductivity, AgNWs maintain good conductivity under bending, twisting, and stretching. MNs were designed to be rigid to guarantee a stable and durable structure that could puncture the skin. This rigid structure of MN makes it possible to penetrate the stratum corneum and capture biomarkers in the body fluid. However, the stiffness mismatch between wearable stretchable patches and rigid MNs presents a challenge to integrate them in one patch for real application. To solve this problem, we present a simple thickness-gradient strategy to combine rigid MNs and the stretchable patch (detailed information is provided in the Experimental Section, Fabrication the Rigid-Soft Gate Structure). Tensile test simulation and stretching experiments with rigid MN-loaded thickness-gradient SIS film proved that the MNs loaded in the middle part were stable and did not detach when the patch was stretched from 0 to 100% deformation (Figure S3 and Videos S1 and S2, Supporting Information, detailed information is provided in Note S1, Supporting Information). Benefiting from this combination of stretchable substance and rigid MNs, the developed MN-loaded patch also shows good flexibility with bending and twisting (Figure 1f–i and Video S3, Supporting Information). By using this thickness-gradient strategy, the MN-loaded patch has both rigid MNs to penetrate the skin and a stretchable substance to maintain skin conformability, demonstrating possible applications that can be used for long-term health monitoring.

2.2. Performance of the Na^+ MN-EGFET Biosensor

The sensing performance of Na^+ MN-EGFET sensor, which exibits high skin conformability (**Figure 2**a), was evaluated by applying Na^+ solutions from 10 to 160×10^{-3} M, considering that the normal average concentration of the Na^+ in ISF is $\approx 145 \times 10^{-3}$ M.[35] The transfer curve shifted to the left with elevated sodium concentrations (Figure 2b), indicating that the sensor was responding to changes in Na^+ concentrations. Elevated response of the drain–source current was also seen with time (Figure 2c), showing a strong linear correlation ($r^2 = 0.987$) in response to the elevated concentrations (Figure 2d). As given by the correlation, the sensitivity is 5.61 mA mM^{-1}, and the LOD is 2.78×10^{-6} M. A brief comparison of the MN-EGFET device with other devices in literature and on the market is presented in Table S1 (Supporting Information). Moreover, the MN-EGFET biosensor gave high repeatability. Elevated sodium concentrations of 10×10^{-3} and 160×10^{-3} M were applied to the sensor within three cycles, leading to a repeatable elevation of the drain–source current response (Figure 2e). The stability of the biosensor is also demonstrated in Video S4 (Supporting Information) and Figure 2f; the biosensor patch was placed on the body and peeled-off along three cycles. The response stayed stable and repeatable over sweep cycles, leading to repeatable and similar current values, thereby proving the high mechanical stability, and sensing reproducibility of the MNs patch when connected and disconnected from the body. Additionally, the long-term stability of the sensor was tested after eight months, showing excellent response and stability (Figure S4, Supporting Information).

The selectivity of the Na^+ biosensor was assessed by applying sodium and other analytes, including K^+, Ca^{2+}, Mg^{2+}, glucose, and cortisol (Figure 2g). The Na^+ biosensor exhibited high selectivity for Na^+ electrolyte, with a current change (ΔI) of 10 ± 2mA, and a low response to the other electrolytes and biomarkers ($K^+ \approx 0.9 \pm 0.8$ mA, $Ca^{2+} \approx 0.2 \pm 0.1$ mA, $Mg^{2+} \approx 0.3 \pm 0.1$ mA, glucose ≈ 0.08 ± 0.07 mA, and cortisol ≈ 0.13 ± 0.07 mA). The stability of the Na^+ biosensor at different pH values was examined in normal ISF pH (7.35–7.45) as well as in a pH regime that s linked with health disorder or disease (pH < 7.35).[36] The sensor exhibited good stability despite changes from pH 5 and pH 7 (Figure 2h), emphasizing that this sensor gives stable measurements when inserted in the ISF regardless of the pH.

In developing the MN-EGFET biosensor, Au was the chosen metal for fabricating the EG electrodes. Besides being biocompatible and nontoxic, one of the prominent advantages of Au electrode is the ability to modify its surface with self-assembled monolayers (SAMs)[37] with different biomolecules such as antibodies and enzymes. Other metals, such as nickel (Ni) and platinum (Pt), could be used for developing the suggested MN-EGFET platform (Figure 2i and Figure S5 and Note 2, Supporting Information).

2.3. Comparison of Microneedle-Based Extended Gate and Flat Biosensor

A comparison with flat EGFET biosensor was carried out to assess the utility and performance of the developed MN-EGFETs. Using MN-EGFET has an advantage over the flat EGFET when it concerns a minimally invasive and immediate method for rapid, continuous, and on-line monitoring and detection of biomarkers in the ISF without the need of exercises for sweating or using sweat extraction methods to

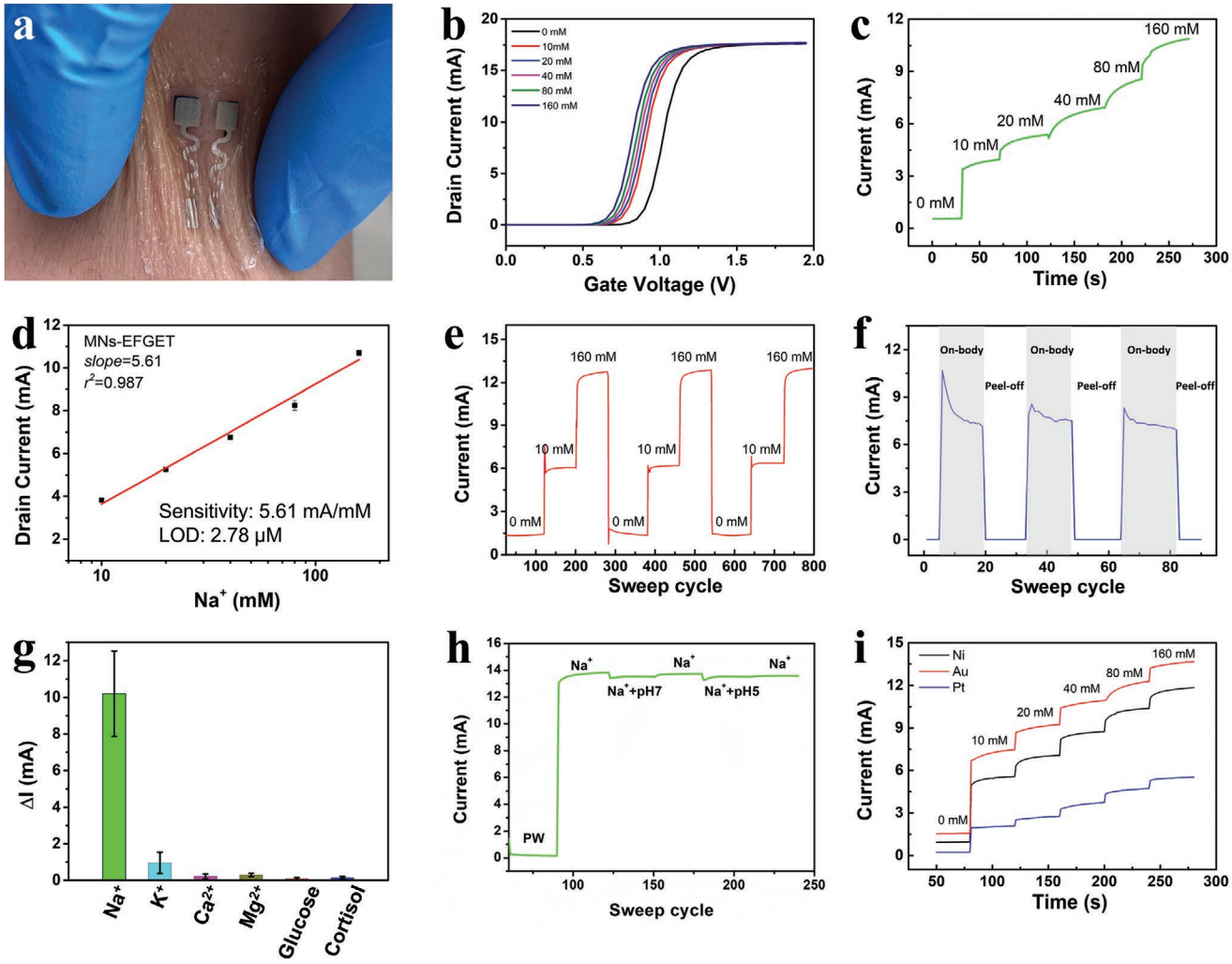

Figure 2. Performance of sodium MN-EGFET biosensor. a) Na^+ MN-EGFET biosensor patch showing high skin conformability. b) Transfer curves of the sensor. c) Drain–source current curve of the sensor in response to elevated sodium concentrations. d) Logarithmic correlation curve of the sensor. e) Repeatability test of the sensor within three cycles. f) Mechanical stability and sensing reproducibility of the sensor. g) Selectivity test for the sensor with different analytes. h) Na^+ sensing stability under different pH. i) Drain–source current curves of the different metal EG-electrodes, Ni (black), Au (red), and Pt (Blue). Sweep cycle refers to the number of voltages sweep from $V_{gs} = 0$ V to $V_{gs} = 2$ V with 0.05 V step.

perform the measurements (Figure S6, Supporting Information). Compared with the sensing performance of the flat EGFET sensor (**Figure 3**a,b, sensitivity: 4.85 mA mM^{-1}; LOD: 30.47×10^{-6} M), the sensitivity of the MN-EGFET sensor is ≈1.16 higher and the LOD is ≈11 times lower. These results emphasize the electrical functional advantage of the MNs over the flat one, and the ability to detect minimal concentrations of biomarkers coupled with higher sensitivity response. Simulation of electric potential proved further the benefits of MNs shape geometry over flat geometry in the ability for connecting more analytes on the surface (Figure 3c,d). A real-time on-body trial was carried out for a more practical comparison (Figure 3e–g and Video S5, Supporting Information). The MNs sensor had an immediate response (in black) 10^8 higher than the flat one (in red). Together these results indicate that the MN-EGFET sensor has better sensing performance, which is very important for real-life applications (detailed information is provided in Note S3, Supporting Information).

2.4. Effect of Confounding Biomarkers on the MN-EGFET Performance

ISF includes a wide variety of other minerals, trace elements, and (bio)chemical compounds that could serve as confounding factors and screen the Na^+-related signals obtained by the MN-EGFET. Modifying the surface of the MN with the appropriate recognition element could solve this issue. For example, four different biorecognition elements were examined to fabricate MN-EGFET biosensors: 1) a sodium selective membrane; 2) polyaniline (PANI); 3) glucose oxidase; and 4) anti-cortisol antibodies. The sensing performance of each sensor was separately characterized with corresponding analyte solutions. PANI exhibited a unique electrical property in which the resistance can be reversibly changed through the protonation and deprotonation process by acid/base. After coating PANI onto the EG, the MN-EGFET platform had a remarkable sensing performance for pH, with 0.85 mA/pH sensitivity (Figure S7a,

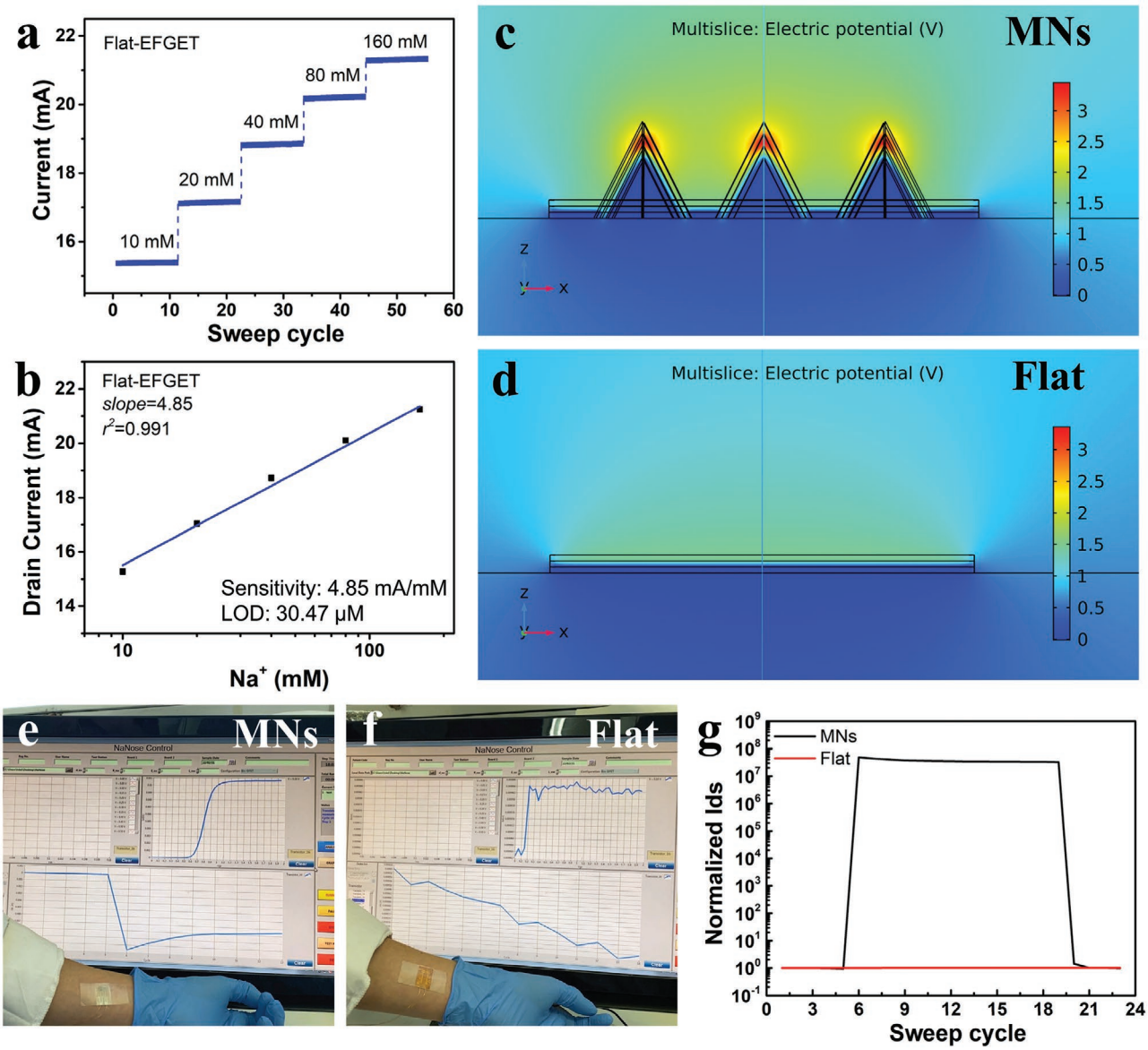

Figure 3. Comparison between flat and MN-EGFET biosensors. a) Drain–source current curve of the flat sensor in response to elevated sodium concentrations. b) Logarithmic correlation curve of the flat sensor. c,d) Electric potential simulation of the MNs and flat biosensors. e,f) Real-time on-body experiment for MNs and flat biosensor patches. g) Normalized response of MNs and flat patches.

Supporting Information). The drain–source current selectively decreased only as the pH increased; meanwhile, only negligible change could be seen when other biomolecules were added, including Na^+, glucose, and cortisol (Figure S7b,c, Supporting Information). The representative current responses of MN-EGFETs coated with glucose oxidase (Figure S7d, Supporting Information) and anti-cortisol antibodies (Figure S7g, Supporting Information) were measured in 0–400 × 10^{-6} M glucose solutions and 0–500 ng mL^{-1} cortisol solutions, respectively. For glucose and cortisol, the drain–source current of each constituent MN-EGFET increased as the corresponding analyte concentration increased (Figure S7e,h, Supporting Information), indicating selectively the corresponding analyte but less to the Na^+ of for the pH. Indeed, the glucose sensor and cortisol sensor also respond to pH (Figure S7f,i, Supporting Information). pH not only affects the activity of the enzyme, but also affects the charge of the antibody, so that the current of both glucose and cortisol sensor changed (21% for glucose and 35% for cortisol) when the pH was taken from pH 7 to pH 5. Altogether, these results indicate the ability to control the selectivity of the Na^+ even under the co-existence of other confounding species in the same ISF source.

2.5. In Vitro and In Vivo Biocompatibility Evaluation of the MNs Patch

Besides the high sensing performance and the wide application range, the biocompatibility of the MNs patch is a fundamental prerequisite for further application in long-term on-body

monitoring. Herein, the biocompatibility of our MNs patch for sodium sensing was systematically evaluated both in vitro and in vivo. Mouse pre-osteoblast MC3T3-E1 cells (CRL-2594) and murine fibroblast NIH3T3 cells (CRL-1658) were cultured with or without the MNs patch for 24 h. Cell viability assay, Live/Dead staining, apoptosis assay, and reactive oxygen species (ROS) assay for cells cultured with or without MNs patch were evaluations carried out separately. There were no statistically significant differences (n = 3 biological replicates) in both MC3T3-E1 and NIH3T3 cells after 24 h culturing with or without the MNs patch, indicating that the patch did not significantly affect cell viability (**Figure 4**a,b). Furthermore, Live/Dead staining of MC3T3-E1 (Figure 4c) and NIH3T3 (Figure 4d) showed that there are living cells, with only a small number of cells dying after 24 h both with and without MNs patches. Further analysis of apoptosis and ROS assays are consistent with the results of both cell viability assay and Live/Dead staining (Figure S8, Supporting Information; detailed information is provided in Note S4, Supporting Information). Together, these results indicate that the MNs patch has no significant impact on the MC3T3-E1 and NIH3T3 cells viability, demonstrating that their excellent in vitro biocompatibility.

To further evaluate the biocompatibility of the MNs patch, MN patches were inserted into the back skin of healthy four-week female BALB/c mice by a thumb press and removed after different insertion times (control, 1 h, 1 d, 3 d, and 7 d). The major organs (including heart, liver, spleen, lung, and kidney) were resected to assess toxicity. Influence on biocompatibility was examined by hematoxylin and eosin (H&E) staining of the organs, together with CD3 immunofluorescent staining assay of skin tissue. No apparent pathological changes and toxic effects were seen in the organs within the different insertion times (Figure 4e), indicating that the MNs patch were not harmful. CD3 is highly expressed in T cells, which are important in the inflammatory response. CD3 immunofluorescent staining of skin tissue from each group after different insertion times also indicated no significant differences between the MNs patch-inserted groups with different inserting time and the control group (Figure S9, Supporting Information). These results show that the MNs patch had no significant impact on the major mice organs and immuno-inflammatory responses, and thus the MNs patch has high potential regarding its in vivo biocompatibility.

2.6. Biocompatibility of the Skin–MN Interface

To evaluate the MNs biocompatibility and its effect on the skin, the possibility of reaching the ISF, and the recovery of the skin following peeling-off, MNs were inserted and removed from mouse skin (**Figure 5**a,b). Microholes appeared after removing the MNs. H&E images showed that the MNs reached the dermis layer, but not the subcutaneous tissues, demonstrating that they have reached the ISF. Subsequently, the microholes disappeared completely within 30 min after removal, and the skin quickly recovered, indicating that the MNs do not damage the skin (Figure 5c). This fast recovery and resealing of the skin is essential to prevent the penetration of pathogenic microbes or toxic substances, reducing the risk of infection. Furthermore, the skin did not show erythema or edema 30 min after MNs removal (Figure 5d), i.e., there was no inflammatory cell infiltration or pathophysiological response of skin upon applying and removing the MNs. This proves that the MNs can reach the ISF within the skin tissue without any inflammatory or toxic response.

2.7. Demonstration of the Wearable Sodium Sensing MNs Patch for On-Body Trial

As the MN-EGFET patch has good sensing performance and excellent biocompatibility, it can be directly used on-body for online and long-term health monitoring. To evaluate the long-term health monitoring performance of the wearable MN-EGFET patch, we used a Na^+ MN-EGFET sensor to perform on-body measurements for several hours of a healthy individual (**Figure 6**a and Figure S10, Supporting Information). As a reference, sweat was collected after exercise and examined by a commercial device (Na^+ meter, HORIBA, B-722) (Figure S11 and Video S6, Supporting Information). Fluctuations in sodium concentration showed a similar tendency to that in the ISF, but with a time delay (Figure 6b). This is because sweat is derived from the interstitial fluid through sweat glands, so that it has a similar sodium concentration fluctuation tendency with ≈40 min delay.[38] Thus, remaining calm is more conducive to obtaining accurate health results, especially with regard to blood pressure, heart rate, electrocardiogram, and blood glucose level. Given the advantage of the MNs, the applied patch can collect health status information of an individual without the need to exercise for sweating, which makes it even more convenient and practical for real-life applications, especially for very sick patients and frail elderly people.

Nowadays, there is an increasing demand for convenient remote healthcare monitoring worldwide. With the help of wireless data communication and IoT technology, frail elderly and sick patients' health status can be measured through biosensors and uploaded onto the IoT cloud by computer/smartphone (Figure 6c). Doctors can readily get the information about the patient and give professional diagnosis without the need for face-to-face consultation, which is more effective and efficient in many cases. To evaluate the applicability of wireless health monitoring with the developed device, the MN-EGFET patch was integrated with a wireless Bluetooth transmitter (ecFlex, Zimmer, and Peacock) by using an additionally designed circuit (Figure S12, Supporting Information). To mimic our body's Na^+ concentration changing, we dropped NaCl solutions onto the Na^+ sensor in the order 10×10^{-3}–40×10^{-3}–160×10^{-3}–10×10^{-3} M. The concentration change was continually recorded, successfully indicating the sodium change by using a smartphone (Figure 6d–f). By integrating with IoT devices, the developed MN-EGFET patch can potentially serve as a health analyzer to monitor an individual's health status, showing great potential for home healthcare and clinical diagnosis. This wearable MN-EGFET platform may provide a new fundamental detection technique through further on-body evaluation.

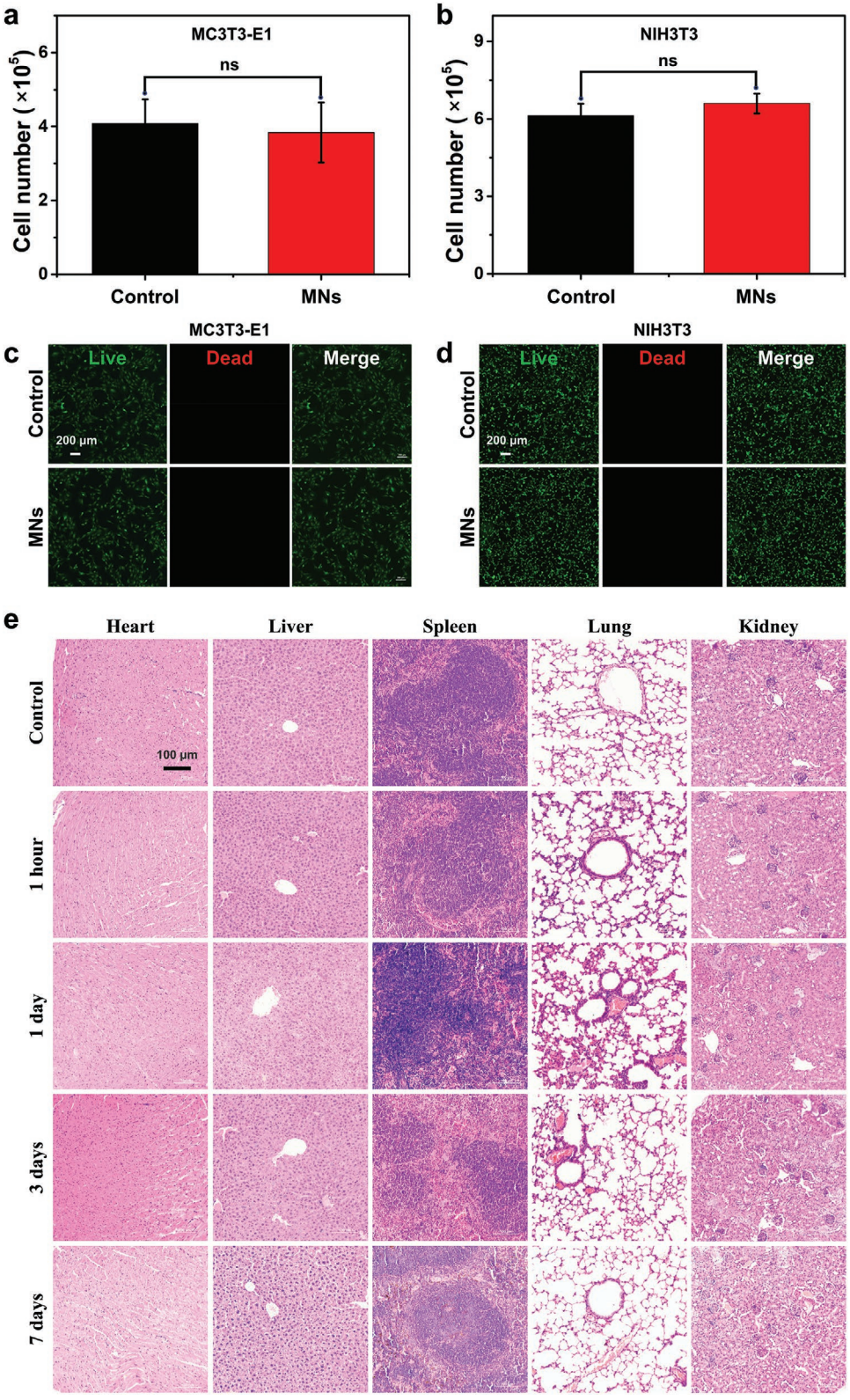

Figure 4. In vitro and in vivo biocompatibility of MNs patch. a,b) Cell number of MC3T3-E1 cells (a) and NIH3T3 cells (b) after 24 h of culturing with/without the MNs patch. c,d) Live/Dead staining of MC3T3-E1 cells (c) and NIH3T3 cells (d) after 24 h of culturing with/without MNs patch. $n = 3$ biological replicates, ns represents no significant difference. e) H&E images of the major organs (heart, liver, spleen, lung, and kidney) of mice with different insertion times of the MNs patch.

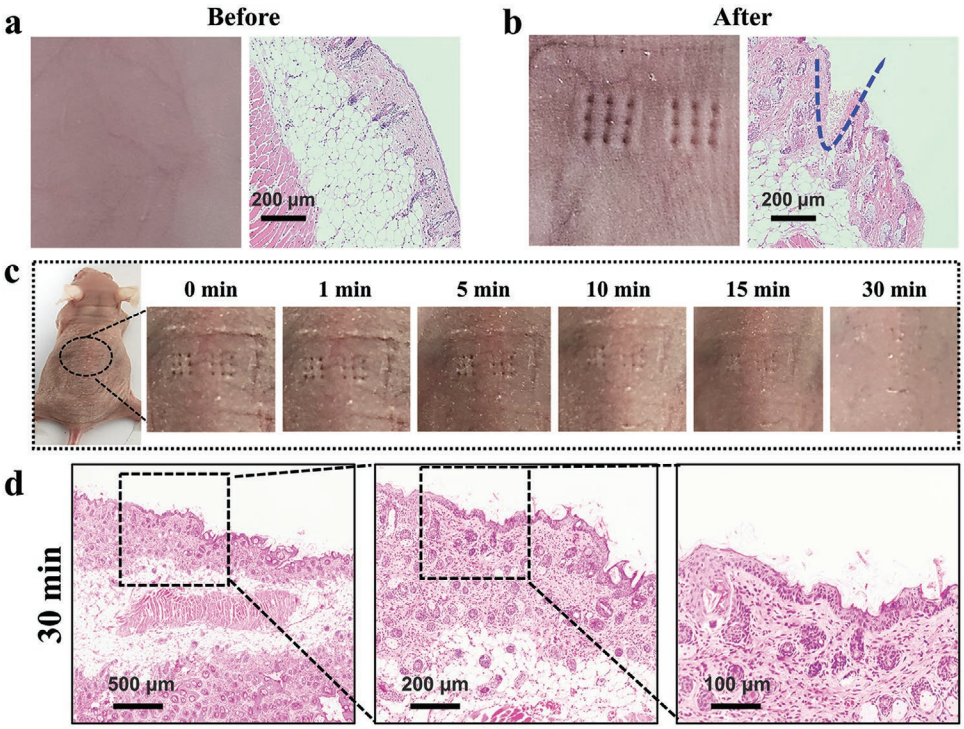

Figure 5. Skin evaluation of the MNs on mice. a,b) Photos and H&E images of the skin tissue of mice before (a) and after (b) insertion of the MNs on the skin. c) Photo of the mice after MNs insertion, including the recovery time after peeling-off the MNs, and the gradual disappearance of microholes over 30 min. d) H&E images of the skin tissue of mice 30 min after MNs removal.

3. Conclusion

This work presents a new stretchable MN-EGFET platform capable of detecting sodium levels in a fast and real-time manner, with no need for extraction processes. This concept can be used to develop a multi-sensing biosensor and be a toolbox for detecting multiple biomarkers with high selectivity, including pH, sodium, cortisol, glucose, and other parameters, by modifying the MNs electrodes with chemical doping, selective membranes, antibodies, and enzymes. The integration of this platform with advanced IoT tools and clinical decision support systems shall serve a shuttling pad for ulimited minimally-invasive health diagnosis and monitoring in both primary and specialized healthcare, thereby reducing the public healthcare costs and lessening the related economic burden.

4. Experimental Section

Materials: Poly(vinylpyrrolidone) (PVP), (3-aminopropyl) triethoxysilane (APTES)-99%, glutaraldehyde (GA)-50%, ethanolamine (EA), 6-mercapto-1-hexanol (MCH), cortisol and anti-cortisol, glucose oxidase (GOx) from *Aspergillus niger*, D (+) glucose, L-cysteine, sodium chloride (NaCl), Dulbecco's phosphate-buffered saline (DPBS), and ethyl glycol solution were purchased from Sigma Aldrich (St. Louis, MO, USA). PDMS and Sylgard 184 Silicone Elastomer Kit were purchased from DOW Inc. (Midland, MI, USA). Resistors and batteries were purchased from Talmir Electronics Ltd. (Haifa, Israel). Live/Dead Cell Imaging Kit was purchased from Thermo Fisher Scientific (Waltham, MA, USA). DAPI and 2′,7′-dichlorodihydrofluorescein diacetate (H2DCFDA) were purchased from Beyotime Biotechnology Company (Shanghai, China). Annexin V-FITC Apoptosis Detection kit was bought by BD Biosciences (Franklin Lake, NJ, USA). Dulbecco's modified Eagle's medium (DMEM) and fetal bovine serum (FBS) were purchased from Gibco (USA). CD3 antibody was purchased from Abcam company (USA). Goat anti-rabbit IgG Alexa Fluor 568 (A11011) was purchased from Thermo Fisher. All chemical solutions were purchased from Bio-Lab Ltd. (Jerusalem, Israel), without any further purification before use. Purified water was used for the preparation of reagents and synthesis. All solutions were prepared using Milli-Q water (18.2 MΩ cm, Millipore, Bedford, MA, USA).

Chemical and Electrical Characterization: A Keithley 2536A System Source meter was used to measure the electrical behavior of the fabricated EGFET sensors. A Zeiss Ultra Plus High-Resolution Cryo-Scanning Electron Microscope (HR-Cryo-SEM) was used to characterize the surface of the fabricated sensors. Universal Laser Systems VersaLASER (VLS) laser cutter was used to create the sensors' shapes and masks.

Synthesis of AgNWs: PVP (2.5 g) was added to 40 mL ethyl glycol solution and mixed with 100 µL 0.15 M $FeCl_3$ in ethyl glycol for 5 min at 160 °C.[39] 100 µL NaCl (0.15 M) was added as a catalyst for the reaction, and then 10 mL 1.5 M $AgNO_3$ was added dropwise while mixing until it preserved a color change of the mixture to light silver. Methanol was added after 2 h to stop the reaction. To obtain the AgNWs, the sample was centrifuged to separate from the other residues. Pure AgNWs were then modified with 1H,1H,2H,2H-perfluorodecanethiol, producing hydrophobic AgNWs–fluorine (AgNWs-F). In brief, 50 mg AgNWs was suspended in 5 mL ethanol/chloroform (1:1 by volume) solution and sonicated for 5 min. 5 µL of 1H,1H,2H,2H-perfluorodecanethiol was added and the mixture was sonicated for 10 min, after which it was kept stirred overnight at 90 °C. To clean the residues, the mixture was centrifuged three times with ethanol/chloroform solution (3000 rpm for 6 min) and dried in a vacuum oven at 50 °C.

Fabrication of MNs: Molds of PDMS for MNs were prepared by carving even holes using a laser cutter. The MNs mold was added to a tube filled with 200 mg mL^{-1} polyester in DMF, then centrifuged at 3000 rpm for 5 min to assist the solution in penetrating and filling the holes. The molds were dried at 80 °C overnight. MNs 3 × 3 array, with

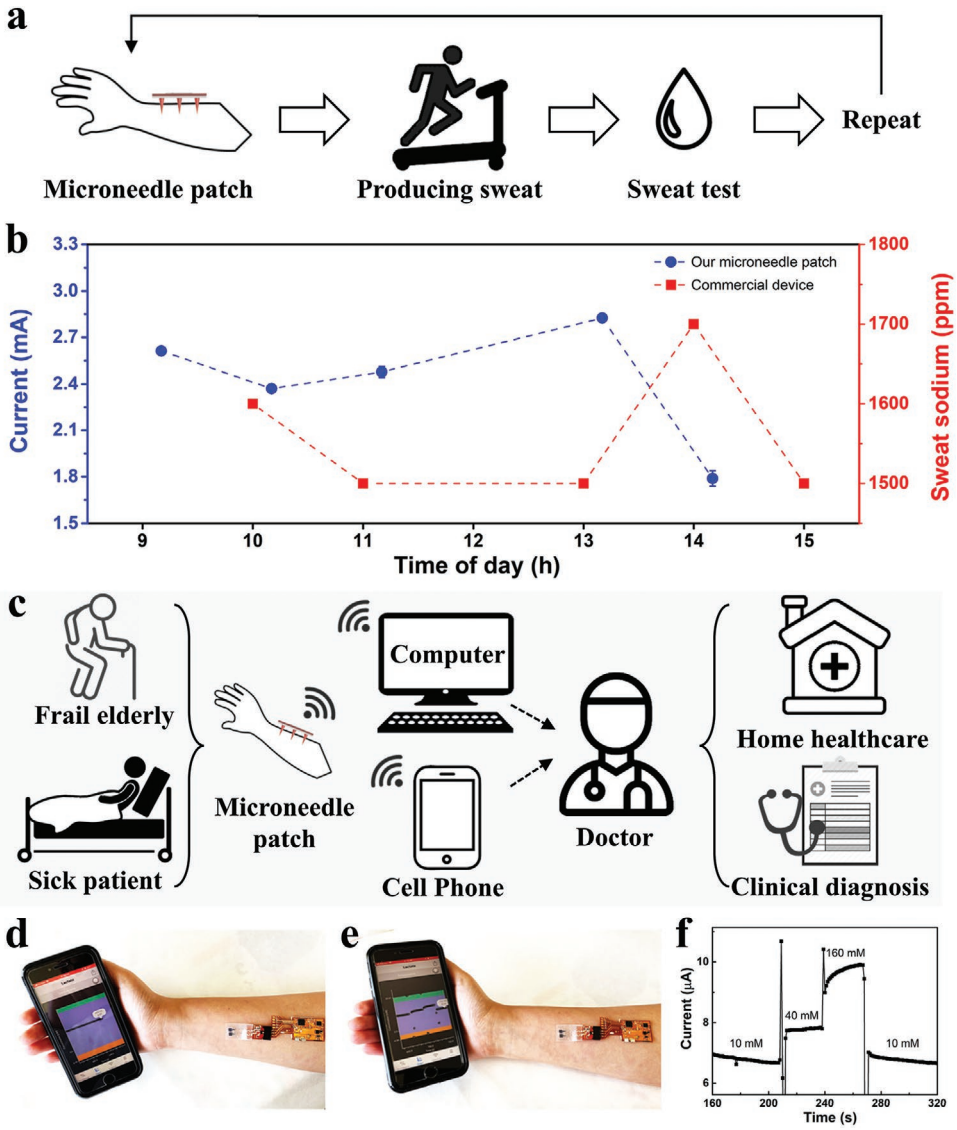

Figure 6. On-body wearable MN-EGFET patch validation. a) Schematic procedures of on-body study of Na^+ sensing using the wearable MN-EGFET patch. b) Long-term monitoring of Na^+ concentration in ISF. The blue dashed line is the readout of MNs patch from ISF, and the red dashed line is the readout of a commercial device from sweat. c) Concept of the wearable MN-EGFET patch for wireless health monitoring in the field of home healthcare and clinical diagnosis. d) Wireless Na^+ detection of 10×10^{-3} M sodium concentration. e) Wireless Na^+ detection in the order of 10×10^{-3}–40×10^{-3}–160×10^{-3}–10×10^{-3} M concentrations. f) Detection data wirelessly transmitted to the smartphone.

a needle length of 1000 μm and a width of 500 μm, were obtained. After demolding, the MNs were deposited with Ag and Au layer separately. Ag/AgCl reference electrodes were obtained by drop-casting 10 μL 0.05 M $FeCl_3$ solution on top of the Ag reference electrode for 1 min, which was then washed with deionized water. A solution of NaCl and poly(vinyl butyral) (PVB) in methanol was added before being vacuum-dried for 30 min to coat the reference electrode.

Fabrication of Na^+ Sensor: 10 mg Na ionophore X were mixed with 5.5 mg sodium tetrakis[3,5-bis(trifluoromethyl)phenyl] borate (Na-TFPB), 33 mg poly(vinyl chloride) (PVC), and 654.5 mg bis(2-ethylehexyl) sebacate (DOS) and dissolved in 6.6 mL tetrahydrofuran (THF). The solution was stored at 4 °C overnight and then 5 μL was drop-cast onto the extended gate electrode.

Cortisol Sensor: The Au gate electrode was first cleaned using ethanol and then with pure water before being thoroughly dried. Immobilization of the monoclonal anti-cortisol was accomplished on the gate by the APTES-GA method.[40] First, the electrode was immersed in 50×10^{-3} M 6-mercapto-1-hexanol (MCH) in ethanol overnight to get an electrode surface with OH terminals, due to the fact that thiol groups come together to create a SAM on the surface of Au.[41] The electrode was washed with ethanol and purified water. It was then immersed in 5% APTES in a solution of 95% ethanol for 2 h, and cleaned with ethanol and water. As cross-linker, GA 2.5% was applied to the electrode for 1 h and then washed with water. The antibodies (1 mg mL^{-1} in Tris-HCl buffer, pH 8) were applied for 2 h. Finally, 100×10^{-3} M EA was added to block the free sites and prevent the nonspecific binding of other molecules.

Glucose Sensor: Chitosan was dissolved in 2% acetic acid by stirring for 1 h to prepare 1% chitosan; 1 mL of the solution was then mixed with 2 mg of carbon nanotubes and ultrasonicated for 30 min. 30 mg mL^{-1} GOx was mixed well in ratio 2:1 (v/v) with the chitosan/CNTs solution. A deposition of a mediator layer of Prussian blue on an Au gate was then made by cyclic voltammetry (CV) versus SCE electrode from –0.2 to 1 V for three cycles with a scan rate of 100 mV s^{-1}. The solution

of GOx/chitosan/CNTs was then drop-cast on the Prussian blue Au gate (5 µL) to get the GOx sensor, which was kept at overnight at 4 °C until use.

pH Sensor: The pH sensor was fabricated by the deposition of PANI by CV versus SCE electrode from −0.5 to 1.5 V for 40 cycles with a rate scan of 100 mV s^{-1}. 0.1 M aniline in HCl was used as deposition solution.

Fabrication the Rigid-Soft Gate Structure: First, an electrode mask was applied on a hydrophobic Si wafer and AgNWs-F were spray-coated. After peeling off the mask, the sprayed AgNWs-F were annealed at 200 °C for 20 min to obtain a conductive AgNWs electrode. 100 mg mL^{-1} SIS in toluene was spin-coated onto the AgNWs electrode with 1000 rpm for 60 s to fabricate a stretchable thin film. This thin film was transferred onto another pre-stretched SIS film prepared in a Teflon template to obtain a stretchable AgNWs electrode (the soft part). To create a variant thickness substance, SIS solution was drop-cast at specific points onto the backside of a prepared stretchable AgNWs electrode to thicken an area on the film (the rigid part). The rigid MNs were then fixed on the rigid part of this thickness-gradient AgNWs electrode film using silver paint. The MNs array (the gate) integrated with the SIS substrate was then combined with the transducer device (SI2302 A2SHB N-Channel MOSFET) to obtain the MN-EGFET platform.

Cell Culture: Mouse pre-osteoblast MC3T3-E1 cells (CRL-2594) and murine fibroblast NIH3T3 cells (CRL-1658) were obtained from American Type Culture Collection (ATCC, USA). MC3T3-E1 cells were cultured in alpha-MEM culture media supplemented with 10% FBS and 1% penicillin-streptomycin at 37 °C with incubation in air plus 5% CO_2. NIH3T3 cells were cultured in DMEM culture media supplemented with 10% FBS and 1% penicillin–streptomycin at 37 °C with incubation in air plus 5% CO_2.

Cell Viability Assay: MC3T3-E1 and NIH3T3 cells were cultured in six-well culture plates (1×10^5 cells per well) overnight before treatment with microneedles for 24 h. The cells were then washed twice with PBS and were collected for direct number assay in a cell counting chamber. Calculation formula: cell number mL^{-1} = (total cell number of the four middle squares/4) $\times 10^4$.

ROS Staining Assay: Cellular ROS was detected by DCFH-DA fluorescence probe. MC3T3-E1 and NIH3T3 cells were cultured in six-well culture plates (1×10^5 cells/well) overnight before treating with the microneedles for 24 h. The cells were then washed twice with PBS and stained with 10×10^{-6} M DCFH-DA for 30 min. They were observed and photographed using a fluorescent microscope (Nikon ECLIPSE Ti-U, Japan).

Live/Dead Staining Assay: MC3T3-E1 and NIH3T3 cells were cultured in six-well culture plates (1×10^5 cells/well) overnight before being treated with microneedles for 24 h. The cells were then washed twice with PBS and stained with the Live/Dead TM Cell Imaging Kit for 30 min. The cells were washed three times with PBS and the living cells or dead cells were photographed by fluorescence microscopy as above.

Apoptosis Assays: MC3T3-E1 and NIH3T3 cells were cultured in six-well culture plates (1×10^5 cells/well) overnight before being treated with the microneedles for 24 h. The cells were twice washed with PBS and stained with Annexin V-FITC for 15 min and PI staining solution for 10 min. After stimulation, the apoptotic cells were analyzed by flow cytometry (BD Biosciences).

In Vivo H&E Toxicity Analysis: For the investigation of in vivo toxicity, healthy four-week female BALB/c mice were treated with the microneedles for different times. The mice were euthanized and their major organs (heart, liver, spleen, lung, and kidney) were collected to assess the toxicity using H&E staining.

CD3 Immunofluorescent Staining Assay of Skin Tissue: Healthy four-week female BALB/c mice were purchased from animal laboratory center of Guangdong province and housed in a SPF laboratory animal room. The mice were treated with the microneedles for different times, and euthanized so that skin could be separated and embedded into OCT agent prior to being sectioned at 5 µm for further immunofluorescent staining. Frozen sections were treated with 4% paraformaldehyde and 0.3% Triton X-100 solution. The frozen sections were blocked with 2% BSA solution for 30 min and incubated with anti-CD3 antibody (ab135372) overnight. On the second day, the frozen sections were washed with 1× TBST for three times and incubated with goat anti-rabbit IgG Alexa Fluor 568 (A11011, Thermo Fisher) for 60 min. The frozen sections were treated with antifade mounting medium with DAPI (H-1200) and imaged with a confocal microscope (Nikon A1R, Japan).

Skin Recovery Ability of the MNs: Healthy four-week female BALB/c mice were treated with the microneedles. The microholes on the mice were photographed after microneedle insertion and removal. After being euthanized, the skin of the mice was collected for H&E assay.

Statistical Analysis: Quantitative data were expressed as mean ± standard deviation (SD). Statistical differences were assessed using one-way analysis of variance (ANOVA). $p < 0.05$ was considered statistically significant.

Ethical Statement: All animal and human experiments were supervised by the medical research ethics committee of the Eighth Affiliated Hospital, Sun Yat-sen University (Futian, Shenzhen)—ZDFBKYLL 2021-023-01 for animal experiment and ZDFBKYLL 2021-024-02 for clinical research. Volunteers in the human on-body demonstrations in this work took part following informed consent.

Supporting Information

Supporting Information is available from the Wiley Online Library or from the author.

Acknowledgements

Y.Z., R.O., and R.Z. contributed equally to this work. This research received funding from the Phase-II Grand Challenges Explorations award of the Bill and Melinda Gates Foundation (OPP1109493) and Horizon 2020 ICT grant under the A-Patch project. This work was supported by the National Natural Science Foundation of China (No. 81972488). R.O. acknowledges The Ariane de Rothschild Program for the Ph.D. scholarship funding.

Conflict of Interest

The authors declare no conflict of interest.

Data Availability Statement

The data that support the findings of this study are available from the corresponding author upon reasonable request.

Keywords

extended gates, field-effect transistors, interstitial fluids, microneedles, wearable sensors

Received: October 26, 2021
Revised: December 6, 2021
Published online: January 20, 2022

[1] S. M. Doshi, P. Shah, X. Lei, A. Lahoti, A. K. Salahudeen, *Am. J. Kidney Dis.* **2012**, *59*, 222.
[2] H. J. Adrogué, N. E. Madias, *N. Engl. J. Med.* **2000**, *342*, 1493.
[3] G. Liamis, T. D. Filippatos, M. S. Elisaf, *Postgrad. Med.* **2016**, *128*, 299.

[4] J. Hu, Y. Wang, X. Geng, R. Chen, P. Zhang, J. Lin, J. Teng, X. Zhang, X. Ding, *Med. Sci. Monit.* **2017**, *23*, 2408.
[5] P. J. G. M. Voets, N. P. J. Vogtländer, K. A. H. Kaasjager, *J. Clin. Monit. Comput.* **2021**, *35*, 655.
[6] M. Pokaharel, C. A. Block, *Curr. Opin. Crit. Care* **2011**, *17*, 581.
[7] M. Darmon, E. Diconne, B. Souweine, S. Ruckly, C. Adrie, E. Azoulay, C. Clec'h, M. Garrouste-Orgeas, C. Schwebel, D. Goldgran-Toledano, H. Khallel, A. S. Dumenil, S. Jamali, C. Cheval, B. Allaouchiche, F. Zeni, J. F. Timsit, *Crit. Care* **2013**, *17*, R12.
[8] L. Balling, M. Schou, L. Videbæk, P. Hildebrandt, H. Wiggers, F. Gustafsson, *Eur. J. Heart Failure* **2011**, *13*, 968.
[9] R. M. Oren, *Am. J. Cardiol.* **2005**, *95*, 2.
[10] N. Deubner, D. Berliner, A. Frey, G. Güder, S. Brenner, W. Fenske, B. Allolio, G. Ertl, C. E. Angermann, S. Störk, *Eur. J. Heart Failure* **2012**, *14*, 1147.
[11] X. Zhao, C. Zou, Y. Wang, Y. Zhang, J. Zhang, *J. Cardiac Failure* **2020**, *26*, S82.
[12] C. Atila, C. O. Sailer, S. Bassetti, S. Tschudin-Sutter, R. Bingisser, M. Siegemund, S. Osswald, K. Rentsch, M. Rueegg, S. Schaerli, G. M. Kuster, R. Twerenbold, M. Christ-Crain, *Eur. J. Endocrinol.* **2021**, *184*, 413.
[13] P. Tzoulis, J. A. Waung, E. Bagkeris, Z. Hussein, A. Biddanda, J. Cousins, A. Dewsnip, K. Falayi, W. McCaughran, C. Mullins, A. Naeem, M. Nwokolo, H. Quah, S. Bitat, E. Deyab, S. Ponnampalam, P.-M. Bouloux, H. Montgomery, S. E. Baldeweg, *J. Clin. Endocrinol. Metab.* **2021**, *106*, 1637.
[14] P. J. G. M. Voets, S. C. Frölke, N. P. J. Vogtländer, K. A. H. Kaasjager, *SAGE Open Med.* **2021**, *9*, 205031212110277.
[15] S. Combs, T. Berl, *Am. J. Kidney Dis.* **2014**, *63*, 294.
[16] T. Dhondup, Q. Qian, *Blood Purif.* **2017**, *43*, 179.
[17] L. G. Sun, Y. Hou, Q. F. Xiao, Y. J. Du, *Sci. Rep.* **2017**, *7*, 15949.
[18] J. Kim, A. S. Campbell, B. E.-F. de Ávila, J. Wang, *Nat. Biotechnol.* **2019**, *37*, 389.
[19] K. Kwon, J. U. Kim, Y. Deng, S. R. Krishnan, J. Choi, H. Jang, K. Lee, C.-J. Su, I. Yoo, Y. Wu, L. Lipschultz, J.-H. Kim, T. S. Chung, D. Wu, Y. Park, T.-I. Kim, R. Ghaffari, S. Lee, Y. Huang, J. A. Rogers, *Nat. Electron.* **2021**, *4*, 302.
[20] O. Zohar, M. Khatib, R. Omar, R. Vishinkin, Y. Y. Broza, H. Haick, *VIEW* **2021**, *2*, 20200172.
[21] Y. Y. Broza, X. Zhou, M. Yuan, D. Qu, Y. Zheng, R. Vishinkin, M. Khatib, W. Wu, H. Haick, *Chem. Rev.* **2019**, *119*, 11761.
[22] Q. Lyu, S. Gong, J. Yin, J. M. Dyson, W. Cheng, *Adv. Healthcare Mater.* **2021**, *10*, 2100577.
[23] T. M. Blicharz, P. Gong, B. M. Bunner, L. L. Chu, K. M. Leonard, J. A. Wakefield, R. E. Williams, M. Dadgar, C. A. Tagliabue, R. El Khaja, S. L. Marlin, R. Haghgooie, S. P. Davis, D. E. Chickering, H. Bernstein, *Nat. Biomed. Eng.* **2018**, *2*, 151.
[24] M. Bariya, H. Y. Y. Nyein, A. Javey, *Nat. Electron.* **2018**, *1*, 160.
[25] S. R. Corrie, J. W. Coffey, J. Islam, K. A. Markey, M. A. F. Kendall, *Analyst* **2015**, *140*, 4350.
[26] B. Ciui, A. Martin, R. K. Mishra, B. Brunetti, T. Nakagawa, T. J. Dawkins, M. Lyu, C. Cristea, R. Sandulescu, J. Wang, *Adv. Healthcare Mater.* **2018**, *7*, 1701264.
[27] K. Y. Goud, C. Moonla, R. K. Mishra, C. Yu, R. Narayan, I. Litvan, J. Wang, *ACS Sens.* **2019**, *4*, 2196.
[28] S. Sharma, Z. Y. Huang, M. Rogers, M. Boutelle, A. E. G. Cass, *Anal. Bioanal. Chem.* **2016**, *408*, 8427.
[29] H. Teymourian, F. Tehrani, K. Mahato, J. Wang, *Adv. Healthcare Mater.* **2021**, *10*, 2002255.
[30] H. Wang, G. Pastorin, C. Lee, *Adv. Sci.* **2016**, *3*, 1500441.
[31] L. Ren, S. Xu, J. Gao, Z. Lin, Z. Chen, B. Liu, L. Liang, L. Jiang, *Sensors* **2018**, *18*, 1191.
[32] K. Takeuchi, N. Takama, R. Kinoshita, T. Okitsu, B. Kim, *Biomed. Microdevices* **2020**, *22*, 79.
[33] M.-Y. Tsai, N. Creedon, E. Brightbill, S. Pavlidis, B. Brown, D. W. Gray, N. Shields, R. Sayers, M. H. Mooney, A. O'Riordan, E. M. Vogel, *Appl. Phys. Lett.* **2017**, *111*, 073701.
[34] L. Rao, P. Wang, Y. Qian, G. Zhou, R. Nötzel, *ACS Omega* **2020**, *5*, 32800.
[35] I. Kurtz, M. K. Nguyen, *Kidney Int.* **2005**, *68*, 1982.
[36] Y. Marunaka, *World J. Diabetes* **2015**, *6*, 125.
[37] C. Vericat, M. E. Vela, G. Benitez, P. Carro, R. C. Salvarezza, *Chem. Soc. Rev.* **2010**, *39*, 1805.
[38] M. G. Bulmer, G. D. Forwell, *J. Physiol.* **1956**, *132*, 115.
[39] B. Wiley, Y. Sun, Y. Xia, *Langmuir* **2005**, *21*, 8077.
[40] N. S. K. Gunda, M. Singh, L. Norman, K. Kaur, S. K. Mitra, *Appl. Surf. Sci.* **2014**, *305*, 522.
[41] C. S. Simsek, M. N. S. Karaboga, M. K. Sezginturk, *Talanta* **2015**, *144*, 210.